



Mapping the wavelength position of mineral features in hyperspectral thermal infrared data

Christoph Hecker^{a,*}, Frank J.A. van Ruitenbeek^a, Wim H. Bakker^a, Babatunde J. Fagbohun^b, Dean Riley^{c,1}, Harald M.A. van der Werff^a, Freek D. van der Meer^a

^a Department of Earth Systems Analysis, Faculty of Geo-Information Science and Earth Observation (ITC), University of Twente, 7514 AE Enschede, the Netherlands

^b Department of Remote Sensing & Geoscience Information System, Federal University of Technology Akure, P.M.B 704, Akure, Nigeria

^c Booz Allen Hamilton, 14151 Park Meadow Dr., Chantilly, VA 20151, USA

ARTICLE INFO

Keywords:

Spectral features
Mineral mapping
Thermal infrared
Longwave infrared
Minimum Wavelength Mapper

ABSTRACT

The *Wavelength Mapper* is an algorithm that searches for the deepest absorption feature in each pixel of a hyperspectral image. On a per pixel basis, it extracts the wavelength position, which serves as a proxy of the mineralogy and the feature depth as a proxy for the relative abundance. This algorithm has been used with near and shortwave infrared data, but has not yet been tested on hyperspectral thermal infrared images. It is unclear what results are expected when the *Wavelength Mapper* algorithm is applied to hyperspectral thermal infrared data since reststrahlen features characteristically overlap in emissivity spectra. In this paper, the *Wavelength Mapper* is tested on a multi-flightline airborne hyperspectral TIR dataset acquired over the Yerington Batholith, Nevada. Observations were made in the 8.05–11.65 μm wavelength range to include thermal spectral features of major rock-forming minerals, and a new color ramp is created to separate quartz-rich rocks from plagioclase-rich rocks. Our results indicate that the *Wavelength Mapper* creates coherent spatial patterns across flightlines. The results displayed represent different types of igneous and sedimentary rocks, as well as the products of hydrothermal alteration via different colors, mainly based on the relative abundance of quartz, feldspar and garnet, as well as mica and epidote. Comparison with published maps indicate that the *Wavelength Mapper* represents for each pixel a parameter value that can be linked to the spectrally dominate rock-forming mineral of that area, as mapped with traditional fieldwork methods. In conclusion, the *Wavelength Mapper* can be applied to airborne hyperspectral TIR data to achieve a simple, repeatable, per-pixel overview map of the dominating rock-forming mineral occurrences.

1. Introduction

Hyperspectral thermal infrared (TIR) images acquired by airborne, ground- or laboratory-based imaging systems are a rapidly developing asset in the toolbox for the spectral geologist. These datasets allow the detection and mapping of non-hydroxylated silicate minerals, such as quartz, feldspars, and garnets, which do not have diagnostic absorption features in the visible to shortwave infrared range (e.g., Feng et al., 2018; Hecker et al., 2010; Riley and Hecker, 2013). Detecting and quantifying rock forming minerals is essential to differentiate and classify igneous, metamorphic, and sedimentary lithologies, (e.g., Aslett et al., 2018; Hecker et al., 2012), as well as their use as indicator minerals for exploration purposes in several deposit models such as porphyry copper systems (Dilles and Einaudi, 1992), iron oxides copper-

gold as well as in Archean gold systems (Marschik and Fontbote, 2001; Robert, 2001) and copper skarns (Cudahy et al., 2001b).

Hyperspectral images contain a large number of bands and require specialized algorithms to extract geologic information. Bakker et al. (2011) and van Ruitenbeek et al. (2014) recently developed a practical tool that maps the wavelength position of the deepest absorption feature. This tool, called “*Minimum Wavelength Mapper*” or “*Wavelength Mapper*” in short, combines the position and depth information of the deepest absorption feature, to give a per-pixel overview map of the dominating mineral occurrences. This process is unsupervised and repeatable, and the results can be interpreted by a geologic expert with limited image processing background.

The *Wavelength Mapper* was originally developed for mapping minerals with different vibrational absorption features in hyperspectral

* Corresponding author.

E-mail address: c.a.hecker@utwente.nl (C. Hecker).

¹ Formerly with The Aerospace Corporation, Chantilly, VA 14745 USA.

shortwave infrared (SWIR) data of Mars (van Ruitenbeek et al., 2014). It was recently used to differentiate minerals with electronic absorption features in the visible to near-infrared region (Hecker et al., 2019). However, no hyperspectral TIR dataset has been tested to date. Reststrahlen features are caused by the fundamental molecular vibrations of the Si-O framework in silicate minerals (e.g., Salisbury et al., 1991) and characteristically overlap each other in different rock-forming minerals in the thermal infrared. Therefore, it is unclear what results are expected when the *Wavelength Mapper* is applied to these reststrahlen features in mineral emissivity spectra in the thermal infrared domain. The aim of this paper is to see if the *Wavelength Mapper* can generate useful information from TIR data. The algorithm was applied on a multiple-flightline dataset of airborne hyperspectral TIR data. The ability of the *Wavelength Maps* in highlighting and mapping mineral distribution patterns of the dominating silicate mineralogy was assessed, and possible adjustments to the method for studies in the thermal domain are discussed.

2. Data

We tested our approach on airborne TIR data that were acquired over Yerington, Nevada during the *Joint Airborne Collection using Hyperspectral Systems* (JACHS; Riley et al., 2008) involving the Aerospace Corporation's SEBASS instrument (midwave and longwave infrared of the TIR) and SpecTIR LLC's ProSpecTIR sensor (Visible to SWIR). The Yerington study area is particularly useful for our test as it contains numerous lithological units and alteration types with infrared-active minerals exposed at the Earth's surface. The Spatially-Enhanced Broadband Array Spectrograph System (SEBASS) is an airborne hyperspectral thermal infrared sensor with exceptionally high signal quality and low noise levels as compared to other thermal sensors (Hackwell et al., 1996; Hecker et al., 2010). SEBASS' LWIR sensor is a push-broom sensor that records spectral radiance in 128 spectral bands (7.6–13.5 μm) and 128 across-track spatial pixels (Hackwell et al., 1996). This aerial survey was flown under clear sky conditions over the Yerington Batholith area between June 17 and 21, 2008. Average altitude was 12,000 feet (ca. 3700 m) above ground level resulting in a nominal ground sample distance of 4 m and a swath width of 550 m. To cover the entire Yerington target area, 36 parallel flightlines were flown in SE–NW direction. Of these, 8 contiguous flightlines were selected that cover a porphyry copper system and its accompanying skarns. For the remainder of the document, we will use thermal infrared or TIR to represent the LWIR section (ca. 8–14 μm) of the electromagnetic spectrum.

2.1. Yerington batholith

The Yerington Batholith in Nevada (Fig. 1) consists of Jurassic multi-phase granitoid intrusions into Triassic-Jurassic volcanic and marine sedimentary units (Dilles et al., 2000). In the Ann-Mason section of the Yerington district (Fig. 2) these host rocks comprise of the middle to late Triassic *McConnell Canyon Volcanics* (andesitic flows with more felsic tops), Triassic-middle Jurassic *Clastic and Evaporitic Sediments* (including carbonates that host the skarns) and a Jurassic eolian *Quartzite*.

In the middle Jurassic, a major magmatic arc developed which produced volcanic eruptions (*Artesia Lake Volcanics*) followed by three major phases of plutonic rocks and porphyry dike swarms, named *McLeod Hill*, *Bear*, and *Luhr Hill*. In the Ann-Mason area, *McLeod Hill* has the most prominent exposure and additionally caused skarn alteration at the contact with the sedimentary units (southern part of the study area). The *Luhr Hill* phase included a porphyry dike swarm that caused typical alteration minerals (Sillitoe, 2010) to form in the affected areas. Expressions of the *Bear* intrusion only occur as the so-called “*Border Phase*” in the study area, which is much more quartz-rich than the surrounding *McLeod Hill* units (pers. comm. J. Dilles, 2012).

The *Singatse Tertiary Volcanics* (Oligocene to early Miocene) overlay these batholithic intrusions with an erosional contact. They consist of an up to 2 km-thick sequence of intermediate to felsic volcanic rocks. During the middle Miocene age, rapid extensional tectonics created several sets of closely-spaced, east-dipping normal faults. This normal faulting contained a rotational component that pivoted the entire pre-Miocene batholithic rock sequences almost 90° to the west. This faulting created the current layout of the Ann-Mason area where the subvolcanic top of the system is outcropping to the west of the area and the Luhr Hill granite cupola at 7 km paleo-depth is situated to the east of the area (Dilles et al., 2000).

As a consequence of its geologic history, the Ann-Mason area contains rock exposures of post-intrusion volcanic rocks to the north; a porphyry system with igneous rocks of variable composition and porphyry alteration mineralogy in the central part; and pre-intrusion volcanic rocks and sediments (partially altered to skarn at the contact with the porphyry system) in the south.

3. Methods

3.1. Pre-processing chain

The airborne data pre-processing chain (described in more detail in Hecker, 2012) contained several steps to suppress noise and atmospheric influences, and transferred the data into apparent emissivity values. In a first step, the last 4 spectral bands were removed as they contained no useful data. Then a destriping algorithm based on the statistics of the individual image columns was applied (Mason, 2002). It replaced bad pixel values and adjusted the gain and offset of the individual cell in the detectors focal plane array (FPA) to match its histogram with those of all the other cells in the same FPA row. This destriped data was then further treated with a denoising approach, using a Minimum Noise Fraction (MNF) transformation (Green et al., 1988) which is similar to a Principal Component Analysis but orders the components by increasing noise levels. Manual inspection revealed that the first ≈ 40 MNF components contained features linked to ground information with increasing levels of noise in the higher components. These 40 components were entered into an inverse MNF transform the MNF components with signal content and reduced noise contributions back into image space. These MNF-denoised images were atmospherically compensated using In-Scene Atmospheric Compensation (ISAC; Young et al., 2002), a simple approach that estimates atmospheric properties based only on scene statistics. These estimated atmospheric properties are assumed to be constant for an entire flightline, but change abruptly between flightlines. The final pre-processing step is the separation of the radiance data into its kinetic temperature and emissivity spectra. We chose the emissivity normalization (ENorm; Kealy and Hook, 1993) approach as it is simple to implement and gives predictable results. The pre-processing was followed by application of the *Wavelength Mapper* (see details in sections 3.2 and 3.3) on the emissivity data of individual flightlines, and the flightlines were combined into a georeferenced mosaics.

3.2. Original wavelength mapper

The *Wavelength Mapper* algorithm is summarized here. The original description can be found in Bakker et al. (2011) and van Ruitenbeek et al. (2014), along with a tutorial including all settings for different applications can be found in Hecker et al. (accepted). The *Wavelength Mapper* was developed for SWIR reflectance data. It works on a pixel-by-pixel basis and consists of two distinct steps:

- Step 1: the wavelength and depth of the deepest absorption feature are determined for each pixel spectrum of the image by parabolic interpolation. This parabolic interpolation allows the algorithm to detect subtle spectral shifts that are smaller than the spacing of the

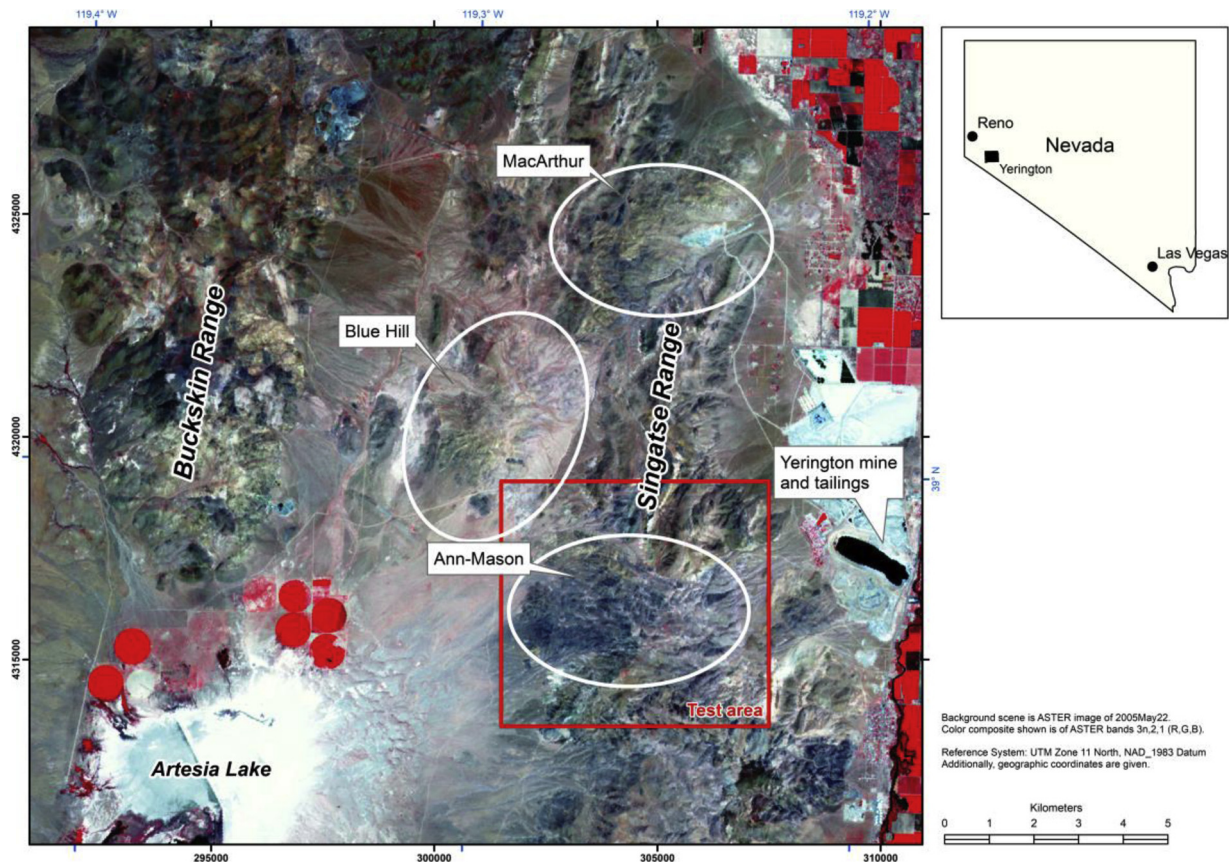


Fig. 1. Overview map of Ann-Mason test area and its spatial relation to other sections of the Yerington Batholith. ASTER near infrared false color composite shows irrigated fields in red, tailings and evaporites in cyan to white and water-filled mine pit in black. The black rectangle in the overview map (inset) indicates location of the main figure. Red frame in main figure (“Test area”) defines extent of Figs. 2, 6 and 7 (For interpretation of the references to colour in this figure, the reader is referred to the web version of this article).

spectral bands.

- Step 2: the determined wavelengths and depths are fused into one map that shows the variation in wavelength positions by different color hues (Fig. 3 left), and the variation in feature depth by different color intensities (“values” in the HSV color system).

Typically, a convex hull is calculated (see Fig. 4) to remove the effect of the continuum on the band position and depth. The continuum is removed by dividing it into the original spectrum assuming that the continuum has a multiplicative effect on the spectrum. Steps 1 and 2 allow setting a spectral subset to guide the algorithm towards the interesting section of the spectra. The Step 1 subset limits the spectral range in which the algorithm seeks for the deepest features, while Step 2 subset adjusts the color stretch of the resulting image to highlight spectral differences.

In the resulting maps, the *Wavelength Mapper* combines the position and depth information of the deepest absorption feature to give a per-pixel overview map of the dominating mineral occurrences in an area. Its strength lies in its simplicity: it requires no *a priori* knowledge of the area, minimal user input, works independent of scene statistics and, as a consequence, gives objective and reproducible results.

However, these products are not classified mineral maps, and require the interpretation by a geologist guided by a look-up table of where minerals have their dominating spectral features. Our practical experience has shown that the spatial patterns resulting from the *Wavelength Mapper* can be easily understood and used as a basis for communicating with geologic experts without formal spectroscopy training.

3.3. Adaptations for TIR

For the airborne TIR images appropriate subset ranges needed to be specified to capture the ranges of the thermal reststrahlen features. Emissivity spectra of the airborne TIR dataset contain a spectral tilt towards shorter wavelengths and some artifacts related to residual atmospheric absorption in the data between 7.5–8.0 μm and beyond 11.7 μm (see Fig. 4). These artifacts have been linked to incomplete atmospheric correction, issues from temperature–emissivity separation algorithms that were developed for lower spectral resolution data, and sensor specific behavior (Cudahy et al., 2001a; Hecker et al., 2016; Vaughan et al., 2005). A balance needed to be achieved between excluding the noisy bands at both ends of the spectral range without omitting spectral features of interest (e.g., the quartz reststrahlen feature). Therefore, we decided on using a **Step 1 range** of 8.05 to 11.65 μm , which preserves the features of carbonates (calcite, dolomite, siderite, and magnesite) at 11.3 μm and most of the reststrahlen features of quartz-rich material (starting at about 7.8 μm), while excluding the noisiest bands.

We used an identical Step 2 range of 8.05 to 11.65 μm to first produce an *overview map* for the entire available TIR spectral range. However, to enhance the differentiation between quartz and plagioclase, a new color scheme was introduced. With quartz having one of the dominant features at 9.2 μm and albitic plagioclase having the deepest feature at 9.6 μm , the shades of the original color scheme are difficult to distinguish. To discern quartz-dominated from plagioclase-dominated areas, a *quartz-plagioclase color scheme* was created that switches abruptly from red to green hues at 9.4 μm (Fig. 3 right).

After the *Wavelength Mapper* step, an outcrop mask was applied to

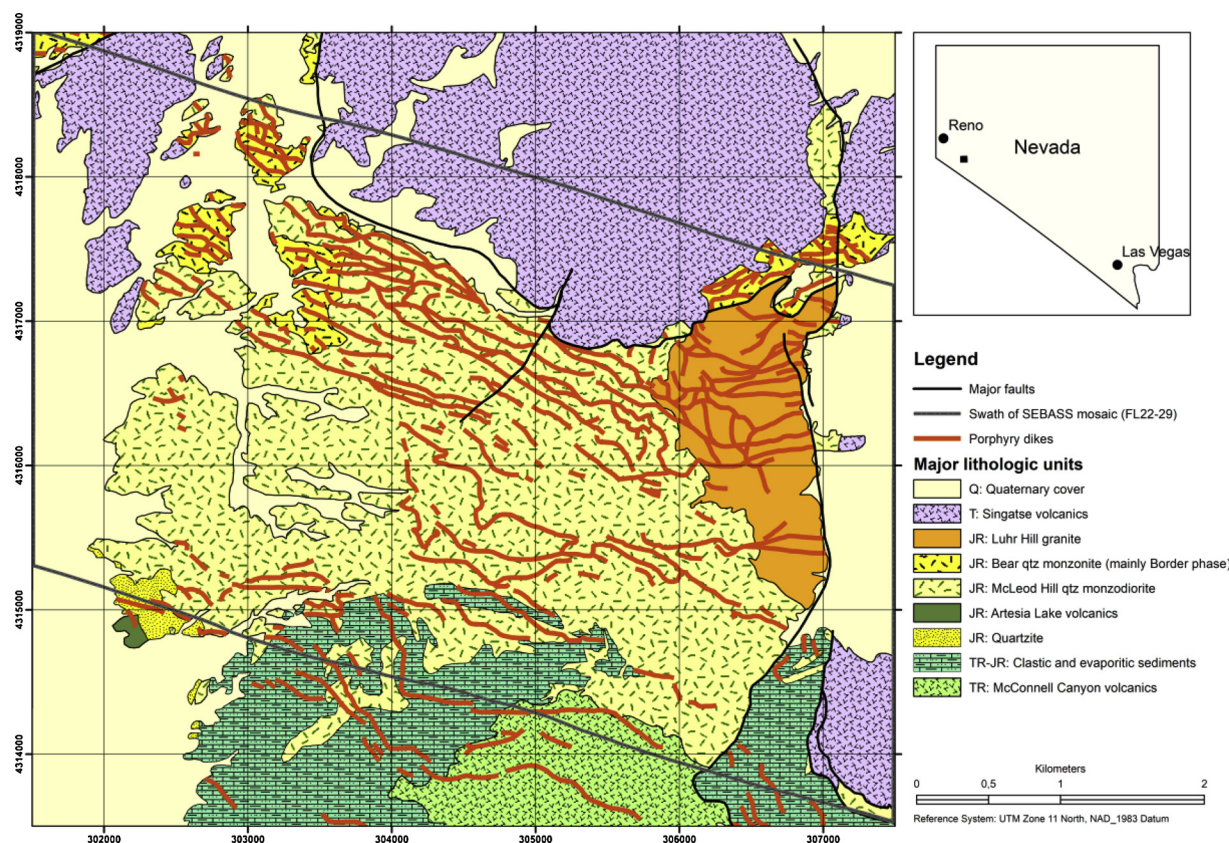


Fig. 2. Generalized geologic map of the Ann-Mason test area, Yerington, Nevada (simplified after Proffett and Dilles (1984)). Gray box indicates the extent of the area covered by airborne TIR data over Ann-Mason (SEBASS mosaic Flightlines 22–29.) The black rectangle in the overview map (inset) indicates location of the main figure.

the resulting maps to mask out areas that are covered by Quaternary cover and to accentuate compositional changes in the bedrock. We sourced the outcrop map from the generalized geologic map of the area (Fig. 2 after Proffett and Dilles, 1984). The masking does not change the results but facilitates comparison with the lithologic units in Fig. 2.

4. Results

The Yerington study area contains altered granitoid intrusions and contact metamorphosed sedimentary units. Typical rock-forming minerals with distinct spectral signatures that can be identified in the TIR airborne images, are quartz, feldspar, epidote, garnet and mica (Fig. 5).

The quartz spectrum was taken from the Jurassic Quartzite unit and the albite spectrum is characteristic for albitized parts of the porphyry copper system. Epidote, garnet and diopside often occur together in

variable amounts in the skarn altered area. Epidote's spectrum was taken from an epidote-rich hornfels and the garnet from the endoskarn. The garnet spectrum shows a distinct peak at 11.4 μm (in Fig. 5 appearing as a plateau due to the end of the spectral range) which indicates Andradite-rich garnet. Minor features at 9.05 and 9.85 μm in the garnet spectrum are indicative of the mineral diopside in the mixture. Spectra of white mica were taken from sericitically altered rocks near the Singatse Fault and from quartz-muscovite-rich pegmatite intrusions, where the former is showing only the 9.0 μm feature but is missing the one at 9.6 μm which is usually also diagnostic for white mica. Fig. 5 illustrates these mineral spectra, and the wavelengths of the deepest spectral features that are targeted in this study (small vertical bars).

Two *Wavelength Mapper* results were produced for this dataset, an overview map and a map for distinguishing quartz and plagioclase-rich areas.

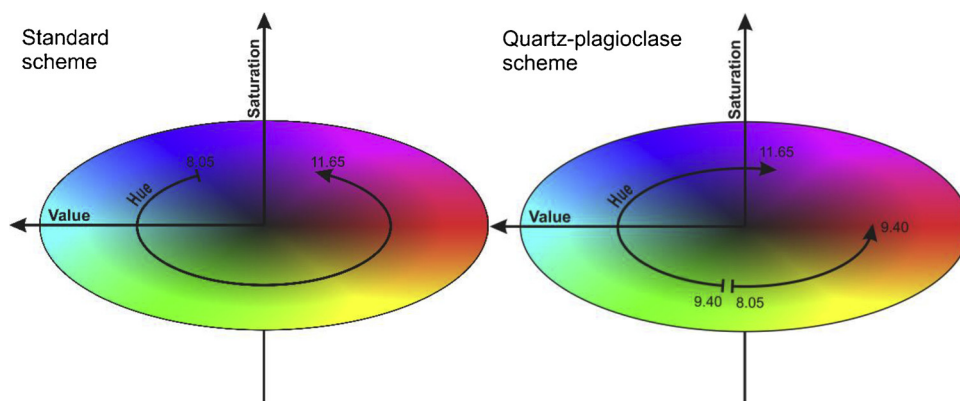


Fig. 3. The standard HSV color scheme (left) utilizes the hues of blue (shortest wavelengths) over green and red to magenta (longest wavelength). The quartz-plagioclase color scheme (right) utilizes the hues of green to red for the shortest wavelengths and continues with green over blue to magenta for the longer wavelengths. This creates an abrupt change in color at the wavelength of 9.40 μm to separate quartz- from plagioclase-dominated pixels (red and green hues, respectively) (For interpretation of the references to colour in this figure, the reader is referred to the web version of this article).

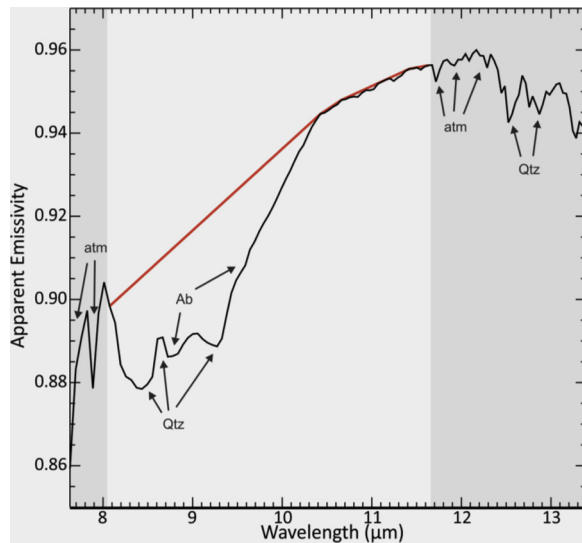


Fig. 4. Example spectrum of the airborne dataset showing spectral features of quartz (Qtz), albitic feldspar (Ab) and residual atmospheric noise (atm). The white background shows the spectral range that was selected for wavelength mapping in the TIR. The red line shows the convex spectral hull continuum that was removed in the wavelength mapping process. Start and end points of the convex hull coincide with the start and end points of the spectral range used (For interpretation of the references to colour in this figure, the reader is referred to the web version of this article).

An overview map (Fig. 6) gives a synoptic view of dominant minerals active in the TIR, without targeting particular TIR spectral features. These results show coherent patches with similar colors that can be traced across the different flightlines. The color intensities are typically higher on topographic highs and lower in the valley bottoms indicating that these patches are related to surface objects and not related to data artifacts. Comparison with the geologic map (Fig. 2) (and confirmed with the spectral information in the data itself) shows that these patches are in fact related to the lithologic units: plagioclase dominated sections of the Ann-Mason porphyry are shown in shades of grass green, quartz-dominated areas in mint green and skarn-related mineralogy in shades of orange and burgundy (for best color separation see digital versions of figures). High quartz content lithologies that can easily be differentiated are: the Jurassic Quartzite (Fig. 6C), the McConnell Canyon volcanic rock unit (Fig. 6E) which is richer in quartz than the other igneous rock units in the area, and quartz-sericite altered units in the left-central part of the image (Fig. 6A). The skarn area in the southern part of the study area is clearly highlighted in burgundy and cut by quartz-rich, pegmatitic bodies (Fig. 6D mint green dashes). Sections of the “Border Phase” that are plagioclase and quartz-rich (Fig. 6B) cannot be differentiated from mainly quartz-dominated pixels in this *Wavelength Mapper* product since they show up in the same mint green color.

The *quartz-plagioclase map* (Fig. 7) uses the quartz-plagioclase color scheme instead of the standard one. This scheme enhances the separation between the quartz-dominated areas (orange and red hues), plagioclase-dominated areas (green hues) and the skarn areas (now in hues of blue) and this alternative color scheme prevents that quartz and plagioclase both are displayed in similar hues of green. Additionally, separation of quartz-rich units from plagioclase-rich igneous rocks, and variations within the igneous rocks are shown: in the western part of the study area, a unit slightly richer in quartz (“Border Phase” unit) in red sticks out from the underlying dioritic units in green (Fig. 7B). Furthermore, the combination of quartz + sericite (Fig. 7A) has a combined spectral feature (9.05 μm) that has a slightly shorter wavelength feature than quartz by itself (9.11 μm). This causes quartz + sericite pixels to stand out in a slightly more orange tint than the deep red for quartz by itself (Fig. 7E) or quartz + plagioclase (9.21 μm). In

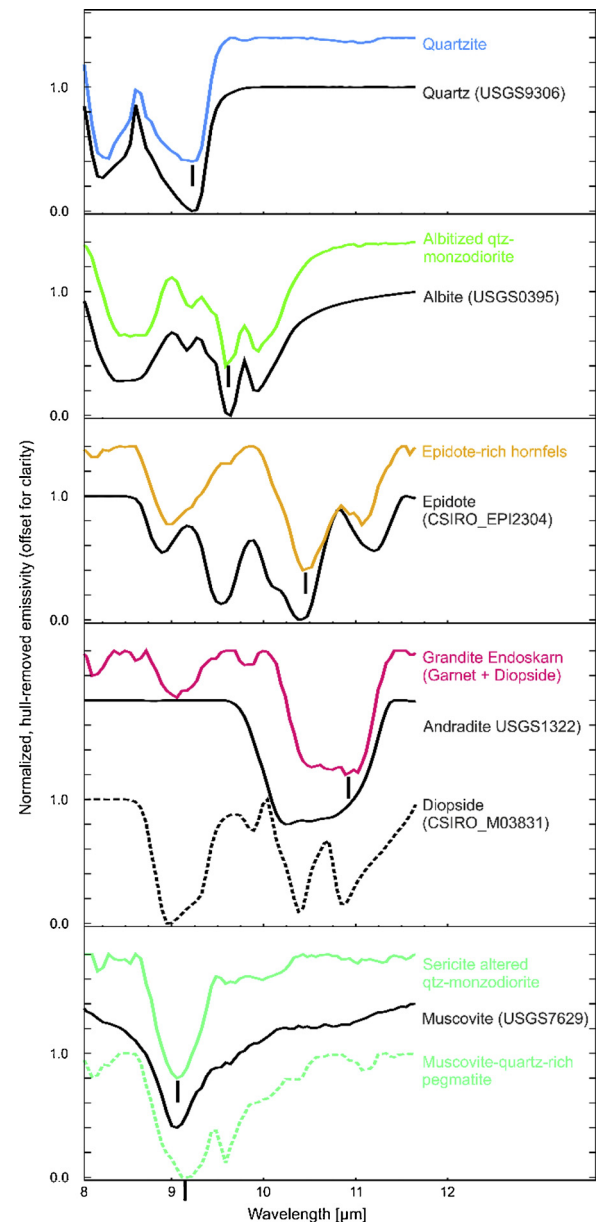


Fig. 5. Examples of image spectra taken from the airborne TIR dataset (colored) for characteristic minerals and mineral combinations in the study area. Library spectra for comparison (in black) were taken from USGS Spectral Library Version7 (Kokaly et al., 2017) and CSIRO reference library (Schodlok et al., 2016). Spectra are continuum-removed and normalized between 0 and 1 to allow comparison between airborne and laboratory spectra with different spectral contrast. Vertical bars indicate position of deepest feature.

the northern and northwestern part of the study area (Fig. 7C), Singatse Tuffs display in burgundy-red hues, indicating a spectral absorption feature of around 9.33 μm . This feature is likely to be caused by the presence of either sanidine or volcanic glass in these tertiary volcanic units (see Byrnes et al. (2007) for spectra of volcanic glass). Furthermore, the skarns and quartz-muscovite-rich pegmatite bodies (Fig. 7D) contrast very well in hues of cyan (epidote-dominated skarn), dark blue (garnet-dominated skarn) and red (quartz-muscovite-dominated pegmatites).

5. Discussion

The findings of this study show that the *Wavelength Mapper* can be adapted to work with airborne TIR data. The *Wavelength Mapper's*

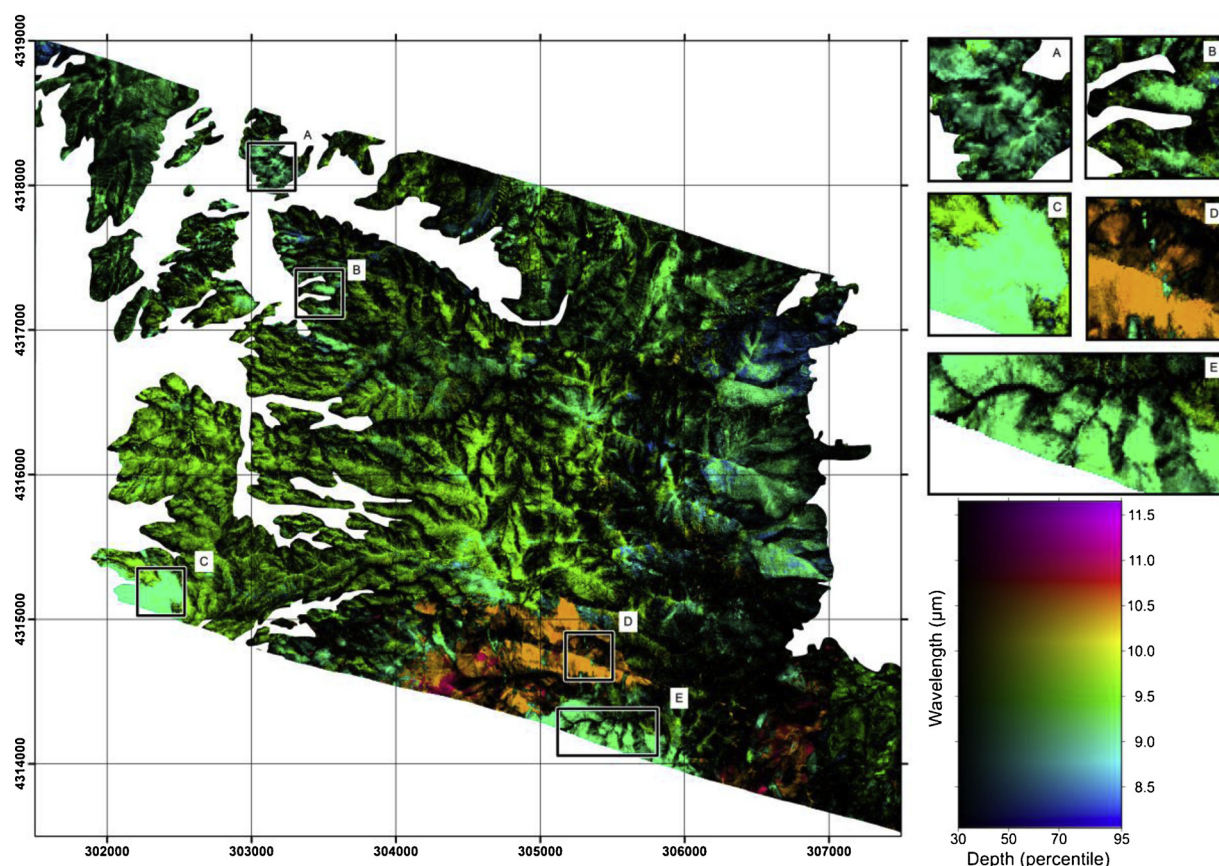


Fig. 6. Overview map of the TIR wavelength mapping results in Ann-Mason. The hues represent the wavelength of the dominant spectral features in the 8.05–11.65 μm range (see legend for the link with wavelength). The color intensity is representing the feature depth and is a proxy for abundance or importance within the pixel. The insets are described in the text (For interpretation of the references to colour in this figure, the reader is referred to the web version of this article).

parameters were adjusted from what is typically used in SWIR applications. The **Step 1 range** of 8.05–11.65 μm was chosen to include the thermal infrared spectral feature of carbonates and (most of) the quartz feature while excluding noisy bands. As most study areas contain quartz- and carbonate-dominated pixels, we consider our Step 1 range a good starting point for most airborne TIR datasets. In cases where data quality allows (in e.g., proximal sensing laboratory setups without atmospheric attenuation), an earlier starting point of 7.8 μm (instead of 8.05 μm used here) could be selected. This would include the entire quartz reststrahlen feature, including the shorter wavelength shoulder or “Christiansen feature” (Salisbury et al., 1991) and a more reliable convex hull fitting without “cutting” into the quartz feature (see Fig. 4).

In the results presented here, the Step 2 range was chosen to match the Step 1 range. However, there are possibilities to vary this setting and get additional results to the overview maps presented here. An example would be the mixtures of quartz with different secondary minerals: In the overview map they all show up as mint green. In the quartz-plagioclase color scheme they all show up as slightly different hues of dark orange and red. However, the exact wavelength position of these features are slightly different, and a Step 2 range of 9.0 to 9.25 μm could differentiate quartz (feature at 9.11 μm) from quartz + sericite (feature at 9.05 μm) and quartz + plagioclase (feature at 9.21 μm).

Additionally, we introduced the alternative *quartz-plagioclase color scheme* to give quartz and plagioclase more “distance” in the color space. This alternative color representation separates these two important minerals much more clearly with a discrete color step, while still preserving the gradual color changes needed in the remaining wavelengths. It appears that some mixtures of plagioclase + quartz are shown in red hues (e.g., Fig. 7B) and linked to quartz even though the

spectrum indicates a dominance of plagioclase. It would be worthwhile to check in the future if a cut-off wavelength of 9.4 μm to separate quartz from plagioclase could be slightly lowered for better spatial discrimination of where plagioclase starts to dominate the mixtures.

These map results show spatial patterns of ground objects that can be traced across flightline boundaries (Figs. 6 and 7). These resulting maps show small artifacts across some flightlines boundaries (i.e., changes mainly in intensity but sometimes also in hue at the edge of a flightline). This is likely caused by the incomplete atmospheric compensation used (i.e., ISAC), which uses individual scene statistics to extract atmospheric parameters and could cause abrupt pixel value changes from one flightline to another.

Under particular circumstances, the same mineral could appear in two different hues in the *Wavelength Maps*. This occurs in minerals with two similarly deep spectral features, such as quartz (see Fig. 5). Minor differences in relative feature depth can cause a pixel in the standard color scheme to either be dark blue (8.4 μm feature is deepest) or mint green (9.2 μm feature is deepest). An example of this effect can be seen in Fig. 6 where quartz-rich areas in the northeastern corner of the study area switch from mint green to blue. This behavior is not specific to TIR data but also occurs in other wavelength ranges when a mineral has several spectral features of similar depth (examples are the 2.2 μm doublet feature of the mineral dickite; or the 1.48 and 2.17 μm features of the mineral alunite). In order to resolve this issue, a tighter subsetting in Step 1 can avoid these interpretative challenges (exclude one of the features from the analysis) as long as that part of the spectral region is not required to separate the minerals of interest.

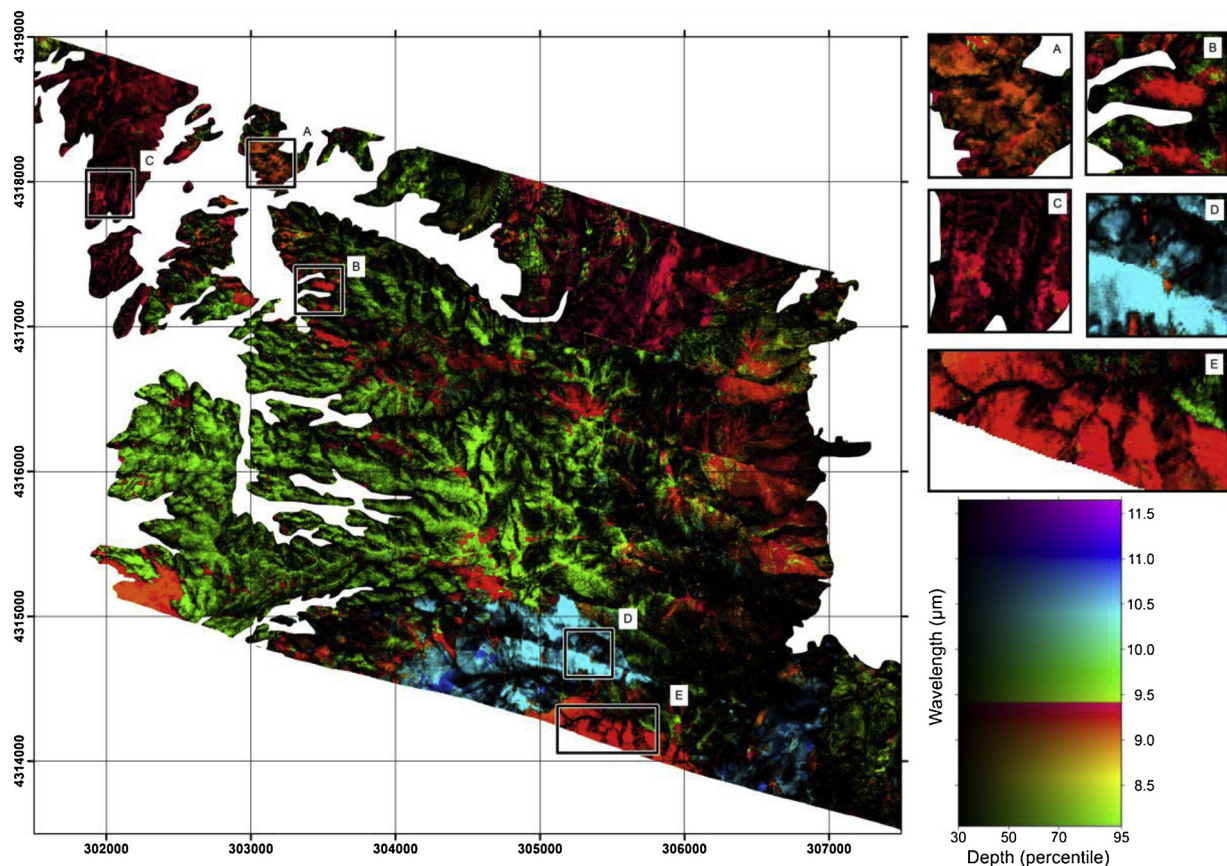


Fig. 7. Quartz-plagioclase map of the TIR wavelength mapping results in Ann-Mason. The settings of the minimum wavelength mapping were identical to those in Fig. 6, but the new quartz-plagioclase color scheme was developed to separate quartz-dominated (red) from plagioclase-dominated (green) pixels. The insets are described in the text (For interpretation of the references to colour in this figure, the reader is referred to the web version of this article).

5.1. Usefulness for silicate mineral mapping

The *Wavelength Mapper* creates output maps highlighting the spectrally dominating TIR mineralogy. The spatial patterns visible in these maps can be linked to the outcropping mineralogy in the study area. Comparison with the lithology map (Fig. 2) shows agreement between the hues in our products and the main lithology and its respective mineral content. Each color hue can be linked to a particular wavelength of the main (i.e., deepest) spectral feature, caused by the spectrally dominating mineralogy in the pixel.

In the TIR airborne data over the Yerington Batholith, the *Wavelength Mapper* separated different types of igneous and sedimentary rocks, as well as the products of hydrothermal alteration minerals, mainly based on the relative abundance of quartz, feldspar and garnet, as well as mica and epidote. Of these, the first three above mentioned minerals are spectrally indistinct in the SWIR range and require the use of the thermal infrared for their detection.

The *Wavelength Mapper* on SWIR datasets uses the absorption wavelength to represent the spectrally dominating mineralogy. Changes in mineral chemistry superimpose additional small wavelength shifts (e.g., van Ruitenbeek et al., 2006 for white mica) which can be detected with the *Wavelength Mapper*. The feature depth, on the other hand, is interpreted as a proxy for mineral abundance. In the thermal infrared the link between mineralogical composition and wavelength, as well as between abundance and depth information is not fully established yet. Research on TIR spectroscopy has shown that feature depth is strongly dependent not only on relative abundance, but also on grain size (Lyon, 1965; Ramsey and Christensen, 1998; Salisbury et al., 1991; Zaini et al., 2012). Changes in mineral chemistry (e.g. plagioclase composition) have shown to create wavelength shifts (e.g., Hecker et al., 2010) as

well as relative depth differences in spectral features (e.g., Cudahy et al., 2009). This study shows that mixed pixels of materials with adjacent spectral features (e.g. sericite, quartz and plagioclase) create spectral features with intermediate wavelength positions, which can be used to visually highlight relative mixtures and their spatial patterns. Future work involving the *Wavelength Mapper* should investigate in detail the link between TIR spectral shapes and the factors that influence it.

The results of the presented case reveal that the *Wavelength Mapper* can be adjusted to work on TIR data. Applying the *Wavelength Mapper* on TIR data is especially useful in situations where a simple approach is needed for a first pass interpretation of mineralogical distribution patterns. If a classified mineral map is needed, an additional interpretation step by a spectral geologist is required.

6. Conclusions

In this paper, we demonstrated the first-time application of the *Wavelength Mapper* to a multi-flightline airborne hyperspectral TIR dataset. Results showed spatial patterns with adequately consistent color and intensity information across the different flightlines. Our adaptations to the TIR range included a definition of the spectral ranges used, as well as a new color scheme to separate the reststrahlen features of quartz and plagioclase.

The spectral subrange (i.e., “Step 1 range”) of 8.05–11.65 μm was selected for this particular airborne image dataset. We recommend this as a starting point for other hyperspectral airborne TIR datasets as well. Care should be taken to check the spectral noise levels at the edge of the atmospheric window near 8 μm . A starting point of 7.8 μm that includes the entire reststrahlen feature of the quartz would be ideal when there

is no atmospheric influence, e.g., with proximal sensing.

We introduced an alternative color scheme with an abrupt color step at 9.4 μm , while preserving the gradual color change for the remainder of the wavelength range covered. This scheme strongly improved the separation of quartz- from plagioclase-dominated pixels in the image into hues of red and green, respectively.

We separated different types of igneous and sedimentary rocks, as well as the products of hydrothermal alteration, mainly based on the relative abundance of quartz, feldspar and garnet, as well as mica and epidote. We observe that the *Wavelength Mapper* represents for each pixel a parameter value that can be linked to the (spectrally) dominating rock-forming mineral of that area as mapped with traditional fieldwork methods. We conclude that the *Wavelength Mapper* can be applied to airborne hyperspectral TIR data to achieve a simple, repeatable, per-pixel overview map of the dominating rock-forming mineral occurrences.

Acknowledgements

The authors would like to thank The Aerospace Corporation and SpectIR LLC for providing the airborne data acquired during the Joint Airborne Collection using Hyperspectral Systems (JACHS) over Yerington, NV, USA. We thank Dr. Martin Schodlok, formerly with CSIRO Exploration and Mining, for providing two mineral spectra and Dr. Robert Hewson for advice on the document. This research was supported by an Internal Research & Development grant from The Aerospace Corporation to Dr. Dean Riley. Babatunde Fagbohun has received funding through the Netherlands Fellowship Programme (NFP). The *Wavelength Mapper* is part of the Hyperspectral Python (HypPy; Bakker et al., 2014) toolbox developed by the University of Twente's Faculty of Geo-Information Science and Earth Observation (UT-ITC). It is an open source tool box written in Python 3 that is free to download from the UT-ITC website (<https://www.itc.nl/grs>).

References

- Aslett, Z., Taranik, J.V., Riley, D.N., 2018. Mapping rock forming minerals at Boundary Canyon, Death Valley National Park, California, using aerial SEBASS thermal infrared hyperspectral image data. *Int. J. Appl. Earth Obs. Geoinf.* 64, 326–339.
- Bakker, W.H., van Ruitenbeek, F.J.A., van der Werff, H.M.A., 2011. Hyperspectral image mapping by automatic color coding of absorption features. 7th EARSEL Workshop of the Special Interest Group in Imaging Spectroscopy 56–57.
- Bakker, W.H., van Ruitenbeek, F.J.A., van der Werff, H.M.A., Zegers, T.E., Oosthoek, J.H.P., Marsh, S.H., van der Meer, F.D., 2014. Processing OMEGA/Mars express hyperspectral imagery from radiance-at-sensor to surface reflectance. *Planet. Space Sci.* 90, 1–9.
- Byrnes, J.M., Ramsey, M.S., King, P.L., Lee, R.J., 2007. Thermal infrared reflectance and emission spectroscopy of quartzofeldspathic glasses. *Geophys. Res. Lett.* 34 (1).
- Cudahy, T.J., Okada, K., Yamato, Y., Cornelius, A., Hewson, R., 2001a. Mapping the Skarn-Porphry-Epithermal Alteration System at Yerington, Nevada, using VNIR-SWIR-TIR Remotely Sensed Data. CSIRO exploration and mining, Floreat Park.
- Cudahy, T.J., Wilson, J., Hewson, R., Linton, P., Harris, P., Sears, M., Okada, K., Hackwell, J.A., 2001b. Mapping porphyry-skarn alteration at Yerington, Nevada, using airborne hyperspectral VNIR-SWIR-TIR imaging data. *International Geoscience and Remote Sensing Symposium (IGARSS)*. pp. 631–633.
- Cudahy, T.J., Hewson, R., Caccetta, M., Roache, A., Whitbourne, L., Connor, P., Coward, D., Mason, P., Yang, K., Huntington, J., Quigley, M., 2009. Drill core logging of plagioclase feldspar composition and other minerals associated with archaic gold mineralization at Kambalda, Western Australia, using a bi-directional thermal infrared reflectance system. In: Bedell, R., Crosta, A.P., Grunsky, E. (Eds.), *Remote Sensing and Spectral Geology. Reviews in Economic Geology. Society of Economic Geologists*, pp. 223–235.
- Dilles, J.H., Einaudi, M.T., 1992. Wall-rock alteration and hydrothermal flow paths about the Ann-Mason porphyry copper deposit, Nevada—a 6 km vertical reconstruction. *Econ. Geol.* 87 (8), 1963–2001.
- Dilles, J.H., Proffett, J.M., Einaudi, M.T., 2000. Magmatic and hydrothermal features of the Yerington batholith with emphasis on the porphyry Cu (Mo) deposit in the Ann-Mason area. In: Dilles, J.H., Barton, M.D., Johnson, D.A., Proffett, J.M., Einaudi, M.T. (Eds.), *Contrasting Styles of Intrusion-Associated Hydrothermal Systems*. SEG, Littleton, pp. 67–90.
- Feng, J., Rogge, D., Rivard, B., 2018. Comparison of lithological mapping results from airborne hyperspectral VNIR-SWIR, LWIR and combined data. *Int. J. Appl. Earth Obs. Geoinf.* 64, 340–353.
- Green, A.A., Berman, M., Switzer, P., Craig, M.D., 1988. A transformation for ordering multispectral data in terms of image quality with implications for noise removal. *IEEE Trans. Geosci. Remote Sens.* 26 (1), 65–74.
- Hackwell, J.A., Warren, D.W., Bongiovanni, R.P., Hansel, S.J., Hayhurst, T.L., Mabry, D.J., Sivjee, M.G., Skinner, J.W., 1996. LWIR / MWIR Imaging Hyperspectral Sensor for Airborne and Ground-Based Remote Sensing. *SPIE* 2819, 102–107.
- Hecker, C.A., 2012. Mapping Feldspars from above: a Thermal Infrared and Partial Least Squares Based Approach. University of Twente Faculty of Geo-Information and Earth Observation (ITC), Enschede 161 pp.
- Hecker, C., van der Meijde, M., van der Meer, F.D., 2010. Thermal infrared spectroscopy on feldspars – successes, limitations and their implications for remote sensing. *Earth. Rev.* 103 (1–2), 60–70.
- Hecker, C., Dilles, J.H., van der Meijde, M., van der Meer, F.D., 2012. Thermal infrared spectroscopy and partial least squares regression to determine mineral modes of granitoid rocks. *Geochem. Geophys. Geosystems* 13, 15.
- Hecker, C., Riley, D., van der Meijde, M., van der Meer, F.D., 2016. Noise simulation and correction in synthetic airborne TIR data for mineral quantification. *IEEE Trans. Geosci. Remote Sens.* 54 (3), 1545–1553.
- Hecker, C., van Ruitenbeek, F.J.A., van der Werff, H.M.A., Bakker, W.H., Hewson, R.D., van der Meer, F.D., 2019. Spectral absorption feature analysis for geological remote sensing applications. *IEEE Geosci. Remote Sens. Mag.* <https://doi.org/10.1109/MGRS.2019.2899193>.
- Kealy, P.S., Hook, S.J., 1993. Separating temperature and emissivity in thermal infrared multispectral scanner data - implications for recovering land-surface temperatures. *IEEE Trans. Geosci. Remote Sens.* 31 (6), 1155–1164.
- Kokaly, R.F., Clark, R.N., Swayze, G.A., Livo, K.E., Hoefen, T.M., Pearson, N.C., Wise, R.A., Benz, W.M., Lowers, H.A., Driscoll, R.L., Klein, A.J., 2017. USGS Spectral Library Version 7: U.S. Geological Survey Data Series 1035. U.S. Geological Survey, Reston, VA, USA.
- Lyon, R.J.P., 1965. Analysis of rocks by spectral infrared emission (8–25 microns). *Econ. Geol.* 60, 715–736.
- Marschik, R., Fontbote, L., 2001. The Candelaria-Punta del Cobre iron oxide Cu-Au-(Zn-Ag) deposits, Chile. *Econ. Geol. Bull. Soc. Econ. Geol.* 96 (8), 1799–1826.
- Mason, P., 2002. MMTG A-List Hyperspectral Data Processing Software. CSIRO Exploration and Mining, North Ryde.
- Proffett, J.M., Dilles, J.H., 1984. Geologic Map of the Yerington District, Nevada. Map 77. Nevada Bureau of Mines and Geology.
- Ramsey, M.S., Christensen, P.R., 1998. Mineral abundance determination: quantitative deconvolution of thermal emission spectra. *J. Geophys. Res.-Solid Earth* 103 (B1), 577–596.
- Riley, D.N., Hecker, C., 2013. Mineral mapping with airborne hyperspectral thermal infrared remote sensing at cuprite, Nevada, USA. In: Kuenzer, C., Dech, S. (Eds.), *Thermal Remote Sensing: Sensors, Methods, Applications*. Springer.
- Riley, D.N., Weatherbee, O., Jones, K.L., Peppin, W.A., 2008. Joint airborne collection using hyperspectral systems (JACHS). Geological and Environmental Mineral Mapping with a Visible-short Wave Infrared and a Mid-wave-long Wave Infrared Hyperspectral Imagers. 33rd International Geological Congress (IGC), Oslo, Norway.
- Robert, F., 2001. Syenite-associated disseminated gold deposits in the Abitibi greenstone belt, Canada. *Miner. Depos.* 36 (6), 503–516.
- Salisbury, J.W., Walter, L.S., Vergo, N., D'Aria, D.M., 1991. *Infrared (2.1–25 μm) Spectra of Minerals*. The Johns Hopkins University Press, Baltimore and London.
- Schodlok, M.C., Green, A., Huntington, J., 2016. A reference library of thermal infrared mineral reflectance spectra for the HyLogger-3 drill core logging system. *Aust. J. Earth Sci.* 63 (8), 941–949.
- Sillitoe, R.H., 2010. Porphyry copper systems. *Econ. Geol.* 105 (1), 3–41.
- van Ruitenbeek, F.J.A., Debba, P., van der Meer, F.D., Cudahy, T., van der Meijde, M., Hale, M., 2006. Mapping white micas and their absorption wavelengths using hyperspectral band ratios. *Remote Sens. Environ.* 102 (3–4), 211–222.
- van Ruitenbeek, F.J.A., Bakker, W.H., van der Werff, H.M.A., Zegers, T.E., Oosthoek, J.H.P., Omer, Z.A., Marsh, S.H., van der Meer, F.D., 2014. Mapping the wavelength position of deepest absorption features to explore mineral diversity in hyperspectral images. *Planet. Space Sci.* 101 (0), 108–117.
- Vaughan, R.G., Hook, S.J., Calvin, W.M., Taranik, J.V., 2005. Surface mineral mapping at Steamboat Springs, Nevada, USA, with multi-wavelength thermal infrared images. *Remote Sens. Environ.* 99 (1–2), 140–158.
- Young, S.J., Johnson, B.R., Hackwell, J.A., 2002. An in-scene method for atmospheric compensation of thermal hyperspectral data. *J. Geophys. Res.* 107 (D24), 4774.
- Zaini, N., van der Meer, F., van der Werff, H., 2012. Effect of grain size and mineral mixing on carbonate absorption features in the SWIR and TIR wavelength regions. *Remote Sens. (Basel)* 4 (4), 987.